

Reconfigurable Low-Threshold All-Optical Nonlinear Activation Functions Based on an Add-Drop Silicon Microring Resonator

Weizhen Yu ¹, Shuang Zheng ¹, Zhenyu Zhao, Bin Wang ¹, and Weifeng Zhang ¹, *Member, IEEE*

Abstract—The realization of optical nonlinear activation functions (NAFs) is essential for integrated optical neural networks (ONNs). Here, we propose and experimentally demonstrate a photonic method to implement reconfigurable and low-threshold all-optical NAFs based on a compact and high-Q add-drop microring resonator (MRR) on silicon. In the experiment, four different NAFs including softplus, radial basis, clamped ReLU, and sigmoid functions are realized by exploiting the thermo-optical (TO) effect of the MRR. The threshold to implement NAFs is as low as 0.08 mW. As a demonstration, a handwritten digit classification benchmark task is simulated based on a convolutional neural network (CNN) using the obtained activation functions, where an accuracy of 98% is realized. Thanks to the unique advantages of ultra-compact footprint and ultralow threshold, the proposed nonlinear unit is promising to be widely used in large-scale integrated ONNs.

Index Terms—Optical neural network, microring resonator, all-optical nonlinear activation functions, thermo-optical effect.

I. INTRODUCTION

IN RECENT years, neuromorphic computing has been attracting considerable attention in a variety of areas, including sensing, robotics, healthcare, and artificial intelligence (AI) [1], [2], [3], [4], [5], [6]. However, the extensive and high-speed computing requirements of neuromorphic computing pose a serious challenge for traditional electrical processors [7], [8]. Compared with digital electronic signal processing, optical signal processing has unique advantages of high speed, low energy consumption, and high parallelism. Optical neural networks

(ONNs), as a novel optical signal processing technique, has been widely investigated in modern neuromorphic computing systems [9], [10], [11], [12], [13], [14]. In general, a neuron in ONNs consists of a linear matrix-vector multiplication (MVM) unit and a nonlinear activation function (NAF) unit. There are already several methods to realize the linear MVM unit, including Mach-Zehnder interferometer (MZI) mesh [15], microring resonator (MRR) weight banks [16], and phase-change material (PCM) array [17].

The NAF unit, which is responsible for nonlinearly mapping the input of the neuron to the output, is capable of enriching the application scenarios of the neural network [18], [19]. In recent years, several photonic approaches have been proposed to realize NAFs [20], [21], [22], [23], [24], [25], [26], [27], [28], [29], [30], [31], [32]. For example, the optical-electrical-optical (O-E-O) method based on electro-absorption modulators [20], [21] and photodetector-modulator structures [22], [23], [24] has been proposed to achieve electro-optical NAFs. This method has potential to achieve reconfigurable NAFs, but it suffers from a large O-E-O conversion loss and a high power consumption. Alternatively, NAFs can also be implemented in the optical domain using all-optical approaches, which have unique advantages of low conversion loss and low power consumption [33]. In the last few years, all-optical NAFs have been implemented in free space [25], using discrete components or semiconductor lasers [26], [27], [28], which can only achieve fixed nonlinear functions. Recently, reconfigurable all-optical NAFs have also been realized based on cavity-loaded MZI structures by exploiting the free carrier dispersion (FCD) effect and the Kerr effect [29], [30]. However, these structures have large footprints of about $10^4 \mu\text{m}^2$ and require a high power threshold of 3 mW. In 2020, an MZI-mesh structure is also proposed to implement different types of NAFs, which has a low threshold of 0.9 mW, but it needs five power supplies to precisely control the phase shift of each phase shifter, which increases the power consumption and the controlling complexity of the chip [31]. Reconfigurable all-optical NAFs, can also be achieved based on a germanium-silicon hybrid integrated MRR, which has a small footprint, but with an increased fabrication complexity [32], making it difficult for mass production. Therefore, an all-optical nonlinear activation unit with a low threshold, a small footprint, and a low fabrication complexity is highly desirable for large-scale integrated ONNs.

Manuscript received 28 September 2022; revised 18 October 2022; accepted 27 October 2022. Date of publication 7 November 2022; date of current version 21 November 2022. This work was supported in part by the National Key Research and Development Program of China under Grant 2019YFB2203303, in part by the National Natural Science Foundation of China (NSFC) under Grant 62071042, in part by the National Natural Science Foundation of China (NSFC) under Grant 62105028, and in part by the China Postdoctoral Science Foundation under Grant 2021M690390. (Weizhen Yu and Shuang Zheng contributed equally to this work.) (Corresponding author: Bin Wang.)

The authors are with the Radar Research Lab, School of Information and Electronics, Beijing Institute of Technology, Beijing 100081, China, also with the Key Laboratory of Electronic and Information Technology in Satellite Navigation (Beijing Institute of Technology), Ministry of Education, Beijing 100081, China, also with the Chongqing Innovation Center, Beijing Institute of Technology, Chongqing 401120, China, and also with the Chongqing Key Laboratory of Novel Civilian Radar, Chongqing 401120, China (e-mail: weizhen.yu@bit.edu.cn; zs_bit@bit.edu.cn; zhenyu.zhao@bit.edu.cn; bin_wang@bit.edu.cn; weifeng.zhang@bit.edu.cn).

Digital Object Identifier 10.1109/JPHOT.2022.3219246

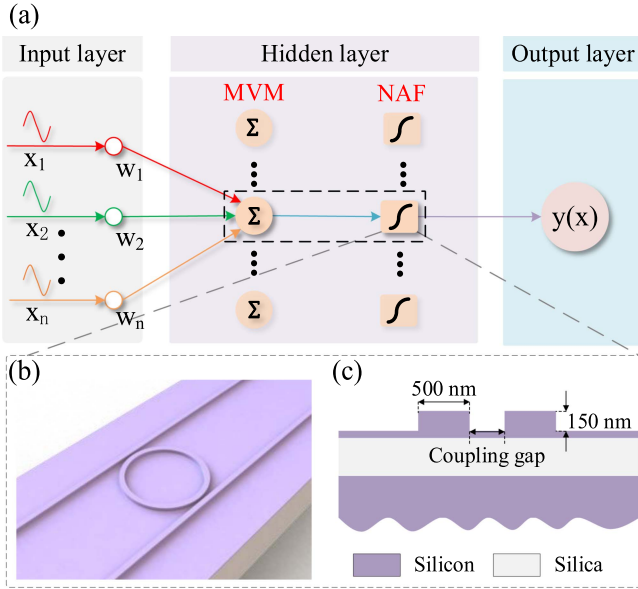


Fig. 1. (a) Optical neurons in the ONN. (b) the schematic of the silicon add-drop MRR. (c) Cross-sectional view of the MRR.

Here, we propose and experimentally demonstrate a novel method to implement various all-optical NAFs with an ultra-compact footprint and a low threshold based on an integrated add-drop silicon MRR. The MRR is fabricated on a standard 220-nm silicon-on-insulator (SOI) platform with a radius of $10 \mu\text{m}$ and a coupling gap of $0.35 \mu\text{m}$. The footprint of the proposed structure is about $10^2 \mu\text{m}^2$. In the silicon platform, the thermo-optical (TO) effect is relatively strong. Up to now, various integrated devices, such as optical switch [34], optical modulator [35], and temperature sensor [36], have already been realized by exploiting the TO effect on silicon. In this work, multiple NAFs including softplus, radial basis, clamped ReLU, and sigmoid functions are implemented based on a TO-tunable MRR, where the wavelength detuning between the optical source and the MRR is controlled properly. For the clamped ReLU function, the nonlinear threshold power is as low as 0.08 mW. Moreover, to verify the applicability of the realized optical NAFs, a handwritten digit classification benchmark task is simulated in a two-layer CNN using the experimentally obtained activation functions, where a test accuracy of 98% is achieved. Benefiting from the unique advantages of ultra-compact footprint and ultralow threshold, the proposed nonlinear unit is promising to be widely used in large-scale integrated ONNs.

II. OPERATION PRINCIPLE

As shown in Fig. 1(a), a neuron in the ONN mainly consists of a linear MVM unit and a NAF unit. The input data can be loaded to the optical domain using an optical modulator. In this work, all-optical NAFs are realized by exploiting the TO effect in a silicon add-drop MRR, as shown in Fig. 1(b). Fig. 1(c) shows the cross-section view of the MRR. The rib waveguide is designed to have a width of 500 nm and an etch depth of 150 nm. As a demonstration, five MRRs are fabricated and

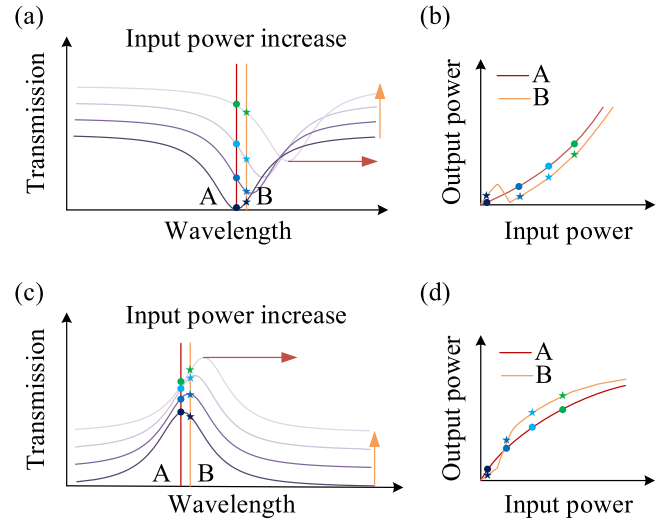


Fig. 2. (a) The schematic of the transmission spectrum at the through port when the input optical power increases. (b) the schematic of all-optical NAFs obtained at the through port. (c) the schematic of the transmission spectrum at the drop port when the input optical power increases. (d) the schematic of all-optical NAFs obtained at the drop port.

evaluated. The radii of the MRRs are $10 \mu\text{m}$, and the coupling gaps are ranging from $0.2 \mu\text{m}$ to $0.4 \mu\text{m}$ with a step of $0.05 \mu\text{m}$.

The realization of all-optical NAFs is based on the nonlinear effects in the silicon add-drop MRR. When light enters the silicon MRR, it will be absorbed due to the two-photon absorption (TPA) effect, which may result in a change in the refractive index of the waveguide. The value of the refractive index change is proportional to the power of the input optical signal (Kerr effect). Through the TPA process, free carriers are also excited, which may lead to free carrier absorption (FCA) and FCD effects. The inter-band and intra-band relaxation effects from carriers generated by TPA and FCA will result in the heating of the structure and lead to a thermal refractive index change. Among these nonlinear effects, the TO effects are dominant, which will result in a redshift of the resonant peak [37].

Fig. 2(a) illustrates the transmission spectrum at the through port of the MRR when the input optical power is increased. It can be observed that the resonant peak of the MRR is redshifted as the input power increases. When the input wavelength is set at the initial resonant wavelength (i.e., A), the output power increases linearly with the input power at a low power level, and then increases rapidly when the input power is high enough to induce a resonant peak redshift. As a result, a softplus NAF is realized, as shown in Fig. 2(b) (line A). When the input wavelength is set at the right side of the initial resonant wavelength (i.e., B), the output power increases linearly with the input power at a low power level. When the input power is high enough to induce a resonant peak redshift, the output power goes through a slump followed by a rapid increase, resulting in a radial basis NAF, as shown in Fig. 2(b) (line B).

Fig. 2(c) illustrates the transmission spectrum at the drop port of the MRR when the input optical power is increased. Firstly, the input wavelength is set at the initial resonant wavelength (i.e., A). When input power increases from zero, the output power

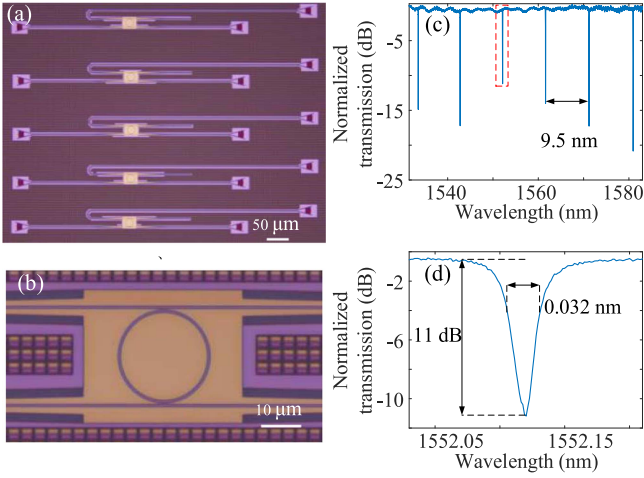


Fig. 3. (a) Microscope image of the fabricated five MRRs with a radius of $10\ \mu\text{m}$ and different coupling gaps. (b) Microscope image of the silicon add-drop MRR with a coupling gap of $0.35\ \mu\text{m}$. (c) the normalized transmission spectrum of the MRR with a coupling gap of $0.35\ \mu\text{m}$. (d) Zoom-in view of the resonance mode near $1552.116\ \text{nm}$.

increases linearly with the input power. When the input power is high enough to induce a resonant peak redshift, the increase of the output power slows down. As a result, a clamped-ReLU NAF is realized at the drop port, as shown in Fig. 2(d) (line A). When the input wavelength is set at the right side of the initial resonant wavelength (i.e., B), the output power firstly increases linearly with the input power at a low power level, which is followed by a rapid increase when the resonant peak redshift occurs. When the input power keeps increasing, the increase of the output power slows down resulting from the deviating of the resonant peak. Consequently, a sigmoid NAF is realized, as shown in Fig. 2(d) (line B).

The TO coefficient of the silicon material is relatively large, which is given by $\partial n/\partial T = 1.86 \times 10^{-4} K^{-1}$. Notably, in a silicon MRR, the light wave is confined in a small footprint, which leads to a low nonlinear excitation threshold. Therefore, a NAF unit with an ultra-compact footprint and an ultralow threshold can be realized based on the silicon MRR structure [37], [38], [39], [40].

III. EXPERIMENTAL RESULTS

Fig. 3(a) shows the microscope image of the fabricated five MRRs, which have a radius of $10\ \mu\text{m}$. The coupling gaps of these five MRRs are $0.2\ \mu\text{m}$, $0.25\ \mu\text{m}$, $0.3\ \mu\text{m}$, $0.35\ \mu\text{m}$, and $0.4\ \mu\text{m}$, respectively. The zoom-in view of the MRR with a coupling gap of $0.35\ \mu\text{m}$ is shown in Fig. 3(b). Fig. 3(c) shows the measured transmission spectrum of this MRR. The free spectral range (FSR) of the MRR is measured to be $9.5\ \text{nm}$. Fig. 3(d) shows the zoom-in view of the resonance mode near $1552.116\ \text{nm}$. The MRR has a 3-dB bandwidth of $32\ \text{pm}$, a Q-factor of 48000 , and an extinction ratio of $11\ \text{dB}$. The insertion loss of the device is measured to be $\sim 12\ \text{dB}$, which includes the fiber-to-fiber I/O coupling loss.

The parameters and performance of these five MRRs, including the radius, the coupling gap, the 3-dB bandwidth, the

TABLE I
THE PARAMETERS OF FIVE DIFFERENT MRRS

	Radius	Gap	3-dB bandwidth	Extinction ratio	Q factor
Ring 1	$10\ \mu\text{m}$	$0.20\ \mu\text{m}$	$0.325\ \text{nm}$	$26\ \text{dB}$	4.7×10^3
Ring 2	$10\ \mu\text{m}$	$0.25\ \mu\text{m}$	$0.130\ \text{nm}$	$26\ \text{dB}$	1.2×10^4
Ring 3	$10\ \mu\text{m}$	$0.30\ \mu\text{m}$	$0.053\ \text{nm}$	$28\ \text{dB}$	2.9×10^4
Ring 4	$10\ \mu\text{m}$	$0.35\ \mu\text{m}$	$0.032\ \text{nm}$	$11\ \text{dB}$	4.8×10^4
Ring 5	$10\ \mu\text{m}$	$0.40\ \mu\text{m}$	$0.015\ \text{nm}$	$10\ \text{dB}$	1.0×10^5

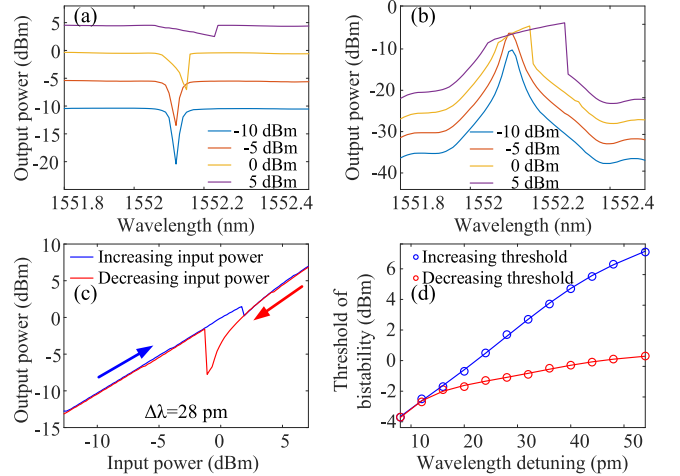


Fig. 4. Measured transmission spectra at (a) the through port and (b) the drop port with different input power. (c) the hysteresis loop relationship between output optical power and input optical power at a fixed wavelength detuning. (d) the extracted power threshold of bistability in the MRR.

extinction ratio, and the Q factor, are shown in Table I. As can be seen, the Q factor increases linearly with the coupling gap. In this work, the MRR with a 3-dB bandwidth of $32\ \text{pm}$, a Q factor of 48000 , and an extinction ratio of $11\ \text{dB}$ is used to implement NAFs.

The transmission spectra at the through port and the drop port of the MRR are measured using a tunable laser source (TLS). In the experiment, when the wavelength of the laser source is set at the initial resonant wavelength, the transmission spectrum of the MRR is redshifted due to the TO effect. Fig. 4(a) and (b) show the measured transmission spectra at the through port and the drop port of the MRR when the optical power is increased from $-10\ \text{dBm}$ to $5\ \text{dBm}$. When the input light wavelength is set at $1552.144\ \text{nm}$, which is far away from the initial resonant wavelength (i.e., $1552.116\ \text{nm}$), the optical bistability phenomenon can be observed. As shown in Fig. 4(c), the hysteresis loop presents the relationships between output power and input power at a $28\ \text{pm}$ wavelength detuning when input power is swept in two opposite directions. At the position of sharp jumping, we can extract the bistability boundary of the input power, which means the threshold of the input optical power to avoid optical bistability. Fig. 4(d) shows the relationship between the wavelength detuning and the power threshold of bistability. As shown in Fig. 4(d), when the wavelength detuning is small (smaller than $16\ \text{pm}$), the increasing threshold matches well with the decreasing threshold, and the curve of the output power remains stable when the input power is increased or decreased.

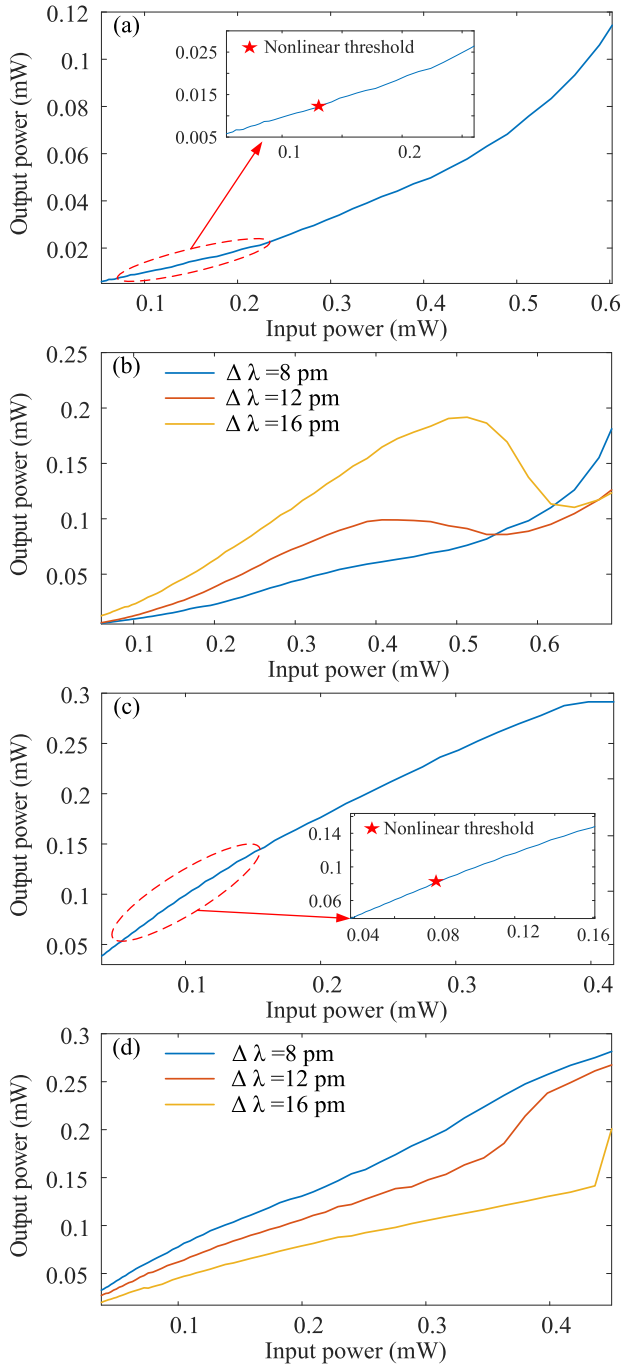


Fig. 5. (a) Measured NAFs at the through port of the MRR when the input optical wavelength is matched with the initial resonant wavelength. (b) Measured NAFs at the through port of the MRR when there is a wavelength detuning. (c) Measured NAFs at the drop port of the MRR when the input optical wavelength is matched with the initial resonant wavelength. (d) Measured NAFs at the drop port of the MRR when there is a wavelength detuning.

In this case, the effect of the optical bistability on the reliability of the NAFs is ignorable.

Fig. 5(a) and (b) show the experimentally measured NAFs at the through port of the MRR. At the initial resonant wavelength, when the input power is at a low level, the output power first increases linearly with the input power since there is almost no redshift. With the continuous increase of the input power,

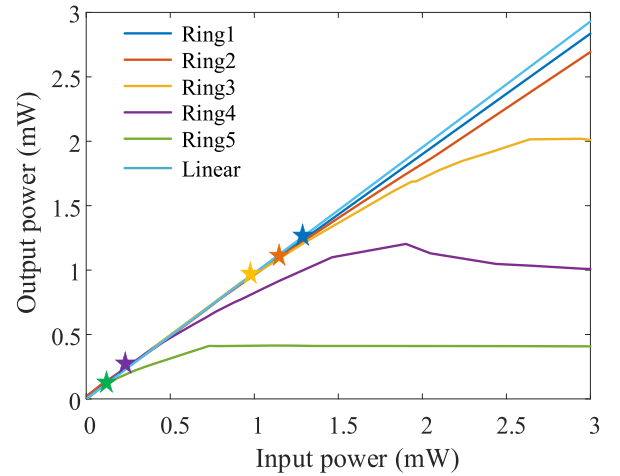


Fig. 6. Measured NAFs at the drop port of the fabricated MRRs with different Q factors.

the resonant peak starts to redshift, resulting in a rapid increase of the output power. Fig. 5(a) shows that a softplus NAF is realized. When the output power increases nonlinearly with the input power, the nonlinear power threshold can be extracted. As shown in the inset of Fig. 5(a), the nonlinear power threshold is measured to be 0.13 mW. When the input wavelength is set to be a bit redshifted from the initial resonant wavelength, the output power first increases with input power at a low power level. Then the output power goes through a drop followed by a rapid increase, which is caused by the redshift of the resonant peak. As a result, a radial basis NAF is realized, as shown in Fig. 5(b).

The experimentally measured NAFs at the drop port of the MRR are shown in Fig. 5(c) and (d). When the input wavelength is set at the initial resonant wavelength, the output power first increases linearly with the input power at a low power level. As the input power keeps increasing, the increase of the output power slows down due to the redshift of the resonant peak. A clamped ReLU NAF is realized, as shown in Fig. 5(c). As given in the inset of Fig. 5(c), the nonlinear power threshold is measured to be 0.08 mW. When the input wavelength is set to be a bit redshifted from the initial resonant wavelength, the output power increases linearly with input power at a low power level. Then the output power goes through a rapid increase, due to the redshift of the resonant peak. When the input power keeps increasing, the increase of the output power slows down resulting from the deviating of the resonant peak. As a result, a sigmoid NAF is realized, as shown in Fig. 5(d).

To evaluate the effect of the Q factor on the implantation of NAFs. The fabricated five MRRs with different Q factors are used to perform NAFs. As shown in Fig. 6, when the input power increases, the output power at the drop port of the MRR is increased nonlinearly. The nonlinear thresholds of these five MRRs are marked in Fig. 6, whose values are 2.95 mW, 1.25 mW, 0.28 mW, 0.18 mW, and 0.08 mW, respectively. As can be seen, the nonlinear power threshold decreases with the increasing Q factor of the MRR.

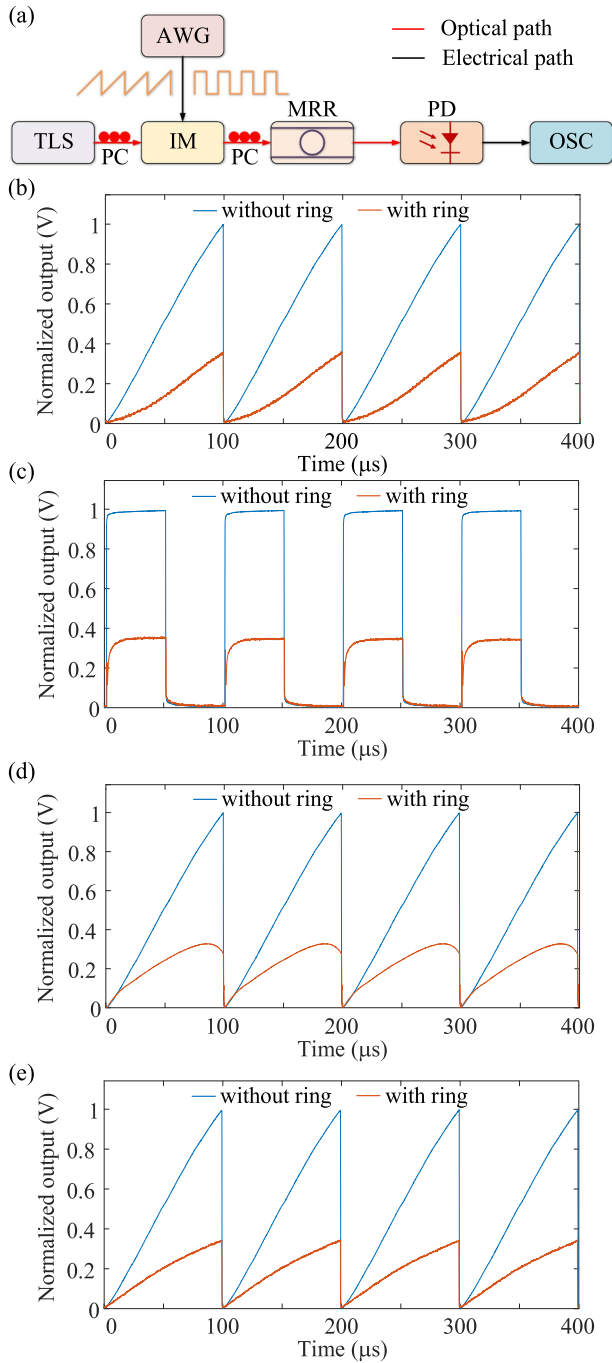


Fig. 7. (a) Experimental setup used to measure the dynamic response of the all-optical NAFs. (b) and (c) are the measured waveforms at the through port of the MRR when the IM is modulated by a sawtooth waveform or a square waveform, respectively. (d) Measured waveform at the through port of the MRR with a wavelength detuning of 16 pm when the IM is modulated by a sawtooth waveform. (e) Measured waveform at the drop port of the MRR when the IM is modulated by a sawtooth waveform.

The dynamic response of the all-optical NAFs is measured based on the experimental setup shown in Fig. 7(a). A continuous-wave (CW) optical signal generated by a TLS is launched into an intensity modulator (IM). Electrical signals generated by an arbitrary waveform generator (AWG) are injected into the IM. The modulated optical signal is fed into the

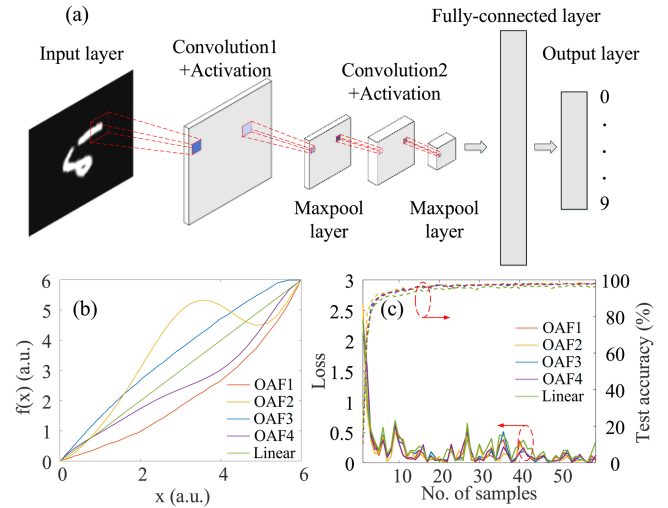


Fig. 8. (a) Schematic of a MNIST handwritten digit classification CNN, comprising convolution, nonlinear activation, maxpooling, and fully-connected layers, resulting in outputs in the range of $[0, 9]$. (b) Different OAFs and linear activation functions used in the simulation. (c) Training loss (left axis) and testing accuracy (right axis) as a function of the number of samples.

MRR, and then detected by a photodetector (PD). The electrical signal generated by the PD is measured by an oscilloscope (OSC). Firstly, a sawtooth signal is sent into the IM and the output signal of the MRR is measured at its through port. The output signal of the modulator is also measured as a reference signal. The output signals are shown in Fig. 7(b), which means that the NAF measured in a dynamic state agrees well with that measured in a static state, as given in Fig. 5(a). Furthermore, to measure the accurate response time, a square wave signal is sent into the device, and the output signals are shown in Fig. 7(c). The rise and fall time are measured to be $\sim 12 \mu\text{s}$, which is the time that the output signal takes to become stable when the input optical power is changed. When the input wavelength is set at the position which is 16-pm redshifted from the initial resonant wavelength, and a sawtooth signal is applied to the MRR, the nonlinear response at the through port is shown in Fig. 7(d). As can be seen, the response curve is in good agreement with the result given in Fig. 5(b). As shown in Fig. 7(e), the measured nonlinear response at the drop port also agrees well with the measured NAF given in Fig. 5(c).

Finally, an MNIST handwritten digit classification task is simulated to verify the applicability of the realized NAFs. The measured four optical NAFs are used as the NAFs in a convolutional neural network (CNN), which are termed as OAF1, OAF2, OAF3, and OAF4 respectively, as shown in Fig. 8. For OAF1 and OAF3, the input optical wavelength is set at the initial resonant wavelength, while for OAF2 and OAF4, the input optical wavelength is detuned from the initial resonant wavelength with a value of 12 pm. Images of handwritten digits with 28×28 pixels are fed into the CNN with two convolutional layers and one fully-connected layer, as shown in Fig. 8(a). A convolution layer includes convolution operation, nonlinear activation operation, and maxpooling operation. The output elements of the fully-connected layer are normalized to represent

TABLE II
COMPARISON OF DIFFERENT ALL-OPTICAL NAFs GENERATION APPROACHES
BASED ON INTEGRATED PLATFORMS

Technologies	Materials	Types	Threshold	Size
MZI-MRR [29]	Si	4	3.16 mW	$10^4 \mu\text{m}^2$
MZI-MRR [30]	SiN	4	3.98 mW	$10^4 \mu\text{m}^2$
MZI mesh [31]	Si	3	0.9 mW	$10^4 \mu\text{m}^2$
Ge/Si MRR [32]	Ge/Si	3	5.1 mW	$10^2 \mu\text{m}^2$
This work	Si	4	0.08 mW	$10^2 \mu\text{m}^2$

probabilities from digit 0 to 9. As shown in Fig. 8(b), a linear function is adopted as a comparison besides OAFs. It should be noticed that the weight and bias of each neuron in the CNN are set to be non-negative due to optical intensity containing no negative value. We perform the simulation on the PyTorch platform, and the AdamOptimizer is used to train the model with a learning rate of 0.001. Fig. 8(c) shows the accuracy of the test dataset and the cross-entropy loss of the training dataset. Within 1 epoch, the CNN converges and an accuracy of 98% is obtained in the test dataset for all OAFs. Compared with the linear function, test accuracy rises from 96% to 98% with our OAFs, and the network converges faster when using OAFs.

IV. DISCUSSION

Table II shows a comprehensive comparison between different all-optical NAFs generation approaches based on integrated platforms. Compared with the MZI-based structures and the Ge/Si-based structures, the proposed add-drop MRR has a smaller footprint, a lower nonlinear threshold, and a lower fabrication complexity. In order to tune the parameters of the NAFs, a planar directional coupler structure [41], or a TO-tuned MZI [42], [43], [44], [45] can be integrated in the MRR, where the coupling coefficient of the MRR can be tuned flexibly. By tuning the coupling coefficient, the Q factor of the MRR can be changed, and the threshold of the NAFs can be changed accordingly. Moreover, the NAFs will also have a much steeper shape when the Q factor of the MRR is increased.

In the experiment, the TO effect (mainly FCA and TPA effects) of a silicon photonic MRR is used to realize the optical NAFs. The all-optical nonlinear response time of the MRR is measured to be 12 μs , which corresponds to a data rate of over 80 kbps. In the future, a much higher data rate up to a few Gbps can be realized by improving the response speed of the MRR with the help of other nonlinear effects, such as FCD and Kerr effects [29], [30]. Meanwhile, self-pulsation is observed in the experiment when the input optical power is high. The NAFs realized in the experiment are all cut off by self-pulsation. Self-pulsation could be further suppressed in MRR by free-carrier depletion [46].

V. CONCLUSION

In this work, we propose and experimentally demonstrate a photonic method to implement reconfigurable and low-threshold all-optical NAFs based on an ultra-compact silicon add-drop MRR. Thanks to the strong TO effect of the MRR, four different types of NAFs are realized by controlling the input wavelength

detuning, including a softplus function and a radial basis function at the through port, a clamped ReLU function and a sigmoid function at the drop port. The nonlinear power threshold is as low as 0.08 mW. Moreover, a handwritten digit classification is simulated in CNN with experimentally measured optical NAFs and obtains an accuracy of 98%. As a purely optical operation unit, the proposed add-drop MRR is promising to be widely used in large-scale integrated ONNs as a reconfigurable nonlinear unit.

REFERENCES

- [1] Y. Hou et al., "Large-scale and flexible optical synapses for neuromorphic computing and integrated visible information sensing memory processing," *ACS Nano*, vol. 15, no. 1, pp. 1497–1508, 2021.
- [2] J. P. Mitchell, G. Bruer, M. E. Dean, J. S. Plank, G. S. Rose, and C. D. Schuman, "NeoN: Neuromorphic control for autonomous robotic navigation," in *Proc. IEEE Int. Symp. Robot. Intell. Sensors*, 2017, pp. 136–142.
- [3] Z. Yu et al., "Hardware-based Hopfield neuromorphic computing for fall detection," *Sensors*, vol. 20, no. 24, 2020, Art. no. 7726.
- [4] M. Davies et al., "Advancing neuromorphic computing with loihi: A survey of results and outlook," *Proc. IEEE*, vol. 109, no. 5, pp. 911–934, May 2021.
- [5] C. D. Schuman et al., "A survey of neuromorphic computing and neural networks in hardware," 2017, *arXiv:1705.06963*.
- [6] F. Steve, "Large-scale neuromorphic computing systems," *J. Neural Eng.*, vol. 13, no. 5, 2016, Art. no. 051001.
- [7] Y. Li, Z. Wang, R. Midya, Q. Xia, and J. Yang, "Review of memristor devices in neuromorphic computing: Materials sciences and device challenges," *J. Phys. D: Appl. Phys.*, vol. 51, no. 50, 2018, Art. no. 503002.
- [8] D. Marković, A. Mizrahi, D. Querlioz, and J. Grollier, "Physics for neuromorphic computing," *Nature Rev. Phys.*, vol. 2, pp. 499–510, 2020.
- [9] B. J. Shastri et al., "Photonics for artificial intelligence and neuromorphic computing," *Nature Photon.*, vol. 15, pp. 102–114, 2021.
- [10] J. Feldmann, N. Youngblood, C. D. Wright, H. Bhaskaran, and W. H. Pernice, "All-optical spiking neurosynaptic networks with self-learning capabilities," *Nature*, vol. 569, no. 7755, pp. 208–214, 2019.
- [11] H. Zhang et al., "An optical neural chip for implementing complex-valued neural network," *Nature Commun.*, vol. 12, no. 1, pp. 1–11, 2021.
- [12] S. Xu et al., "Optical coherent dot-product chip for sophisticated deep learning regression," *Light: Sci. Appl.*, vol. 10, no. 1, pp. 1–12, 2021.
- [13] C. Huang et al., "A silicon photonic–electronic neural network for fibre nonlinearity compensation," *Nature Electron.*, vol. 4, no. 11, pp. 837–844, 2021.
- [14] C. Wu, H. Yu, S. Lee, R. Peng, I. Takeuchi, and M. Li, "Programmable phase-change metasurfaces on waveguides for multimode photonic convolutional neural network," *Nature Commun.*, vol. 12, no. 1, pp. 1–8, 2021.
- [15] Y. Shen et al., "Deep learning with coherent nanophotonic circuits," *Nature Photon.*, vol. 11, no. 7, pp. 441–446, 2017.
- [16] A. N. Tait et al., "Microring weight banks," *IEEE J. Sel. Topics Quantum Electron.*, vol. 22, no. 6, pp. 312–325, Nov./Dec. 2016.
- [17] J. Feldmann et al., "Parallel convolutional processing using an integrated photonic tensor core," *Nature*, vol. 589, no. 7840, pp. 52–58, 2021.
- [18] M. Leshno, V. Y. Lin, A. Pinkus, and S. Schocken, "Multilayer feedforward networks with a nonpolynomial activation function can approximate any function," *Neural Netw.*, vol. 6, no. 6, pp. 861–867, 1993.
- [19] S. Sharma, S. Sharma, and A. Athaiya, "Activation functions in neural networks," *Int. J. Appl. Sci. Eng.*, vol. 4, no. 12, pp. 310–316, 2017.
- [20] R. Amin et al., "ITO-based electro-absorption modulator for photonic neural activation function," *APL Mater.*, vol. 7, no. 8, 2019, Art. no. 081112.
- [21] J. K. George et al., "Neuromorphic photonics with electro-absorption modulators," *Opt. Exp.*, vol. 27, no. 4, pp. 5181–5191, 2019.
- [22] A. N. Tait et al., "Silicon photonic modulator neuron," *Phys. Rev. Appl.*, vol. 11, no. 6, 2019, Art. no. 064043.
- [23] M. M. P. Fard et al., "Experimental realization of arbitrary activation functions for optical neural networks," *Opt. Exp.*, vol. 28, pp. 12138–12148, 2020.
- [24] I. A. D. Williamson, T. W. Hughes, M. Minkov, B. Barlett, S. Pai, and S. Fan, "Reprogrammable electro-optic nonlinear activation functions for optical neural networks," *IEEE J. Quantum Electron.*, vol. 26, no. 1, Jan./Feb. 2020, Art. no. 7700412.

- [25] Y. Zuo et al., "All-optical neural network with nonlinear activation functions," *Optica*, vol. 6, no. 9, pp. 1132–1137, 2019.
- [26] M. Mario et al., "All-optical nonlinear activation function for photonic neural networks," *Opt. Mater. Exp.*, vol. 8, pp. 3851–3863, 2018.
- [27] G. M. Alexandris, A. Tsakyridis, N. Passalis, A. Tefas, K. Vysokinos, and N. Pleros, "An all-optical neuron with sigmoid activation function," *Opt. Exp.*, vol. 27, pp. 9620–9630, 2019.
- [28] T. S. Rasmussen, Y. Yu, and J. Mork, "All-optical non-linear activation function for neuromorphic photonic computing using semiconductor Fano lasers," *Opt. Lett.*, vol. 45, no. 14, pp. 3844–3847, 2020.
- [29] A. Jha, C. Huang, and P. R. Prucnal, "Reconfigurable all-optical nonlinear activation functions for neuromorphic photonics," *Opt. Lett.*, vol. 45, no. 17, pp. 4819–4822, 2020.
- [30] A. Jha, C. Huang, and P. R. Prucnal, "Programmable, high-speed all-optical nonlinear activation functions for neuromorphic photonics," in *Proc. IEEE Opt. Fiber Commun. Conf.*, 2021, pp. 1–3.
- [31] Q. Li et al., "Optical nonlinear activation functions based on MZI-structure for optical neural networks," in *Proc. IEEE Asia Commun. Photon. Conf. Int. Conf. Inf. Photon. Opt. Commun.*, 2020, pp. 1–3.
- [32] B. Wu, H. Li, W. Tong, J. Dong, and X. Zhang, "Low-threshold all-optical nonlinear activation function based on a Ge/Si hybrid structure in a microring resonator," *Opt. Mater. Exp.*, vol. 12, no. 3, pp. 970–980, 2022.
- [33] V. Rutckaia and J. Schilling, "Ultrafast low-energy all-optical switching," *Nature Photon.*, vol. 14, pp. 4–6, 2020.
- [34] H. Yamada, T. Chu, S. Ishida, and Y. Arakawa, "Si photonic wire waveguide devices," *IEEE J. Sel. Topics Quantum Electron.*, vol. 12, no. 6, pp. 1371–1379, Nov./Dec. 2006.
- [35] J. Sun, R. Kumar, M. Sakib, J. B. Driscoll, H. Jayatileka, and H. Rong, "A 128 Gb/s PAM4 silicon microring modulator with integrated thermo-optic resonance tuning," *J. Light. Technol.*, vol. 37, no. 1, pp. 110–115, Jan. 2019.
- [36] N. N. Klimov, S. Mittal, M. Berger, and Z. Ahmed, "On-chip silicon waveguide Bragg grating photonic temperature sensor," *Opt. Lett.*, vol. 40, pp. 3934–3936, 2015.
- [37] G. Priem, P. Dumon, W. Bogaerts, D. Van Thourhout, G. Morthier, and R. Baets, "Optical bistability and pulsating behaviour in silicon-on-insulator ring resonator structures," *Opt. Exp.*, vol. 13, pp. 9623–9628, 2005.
- [38] G. Cocorullo and I. Rendina, "Thermo-optical modulation at 1.5 μm in silicon etalon," *Electron. Lett.*, vol. 1, no. 28, pp. 83–5, 1992.
- [39] V. R. Almeida and M. Lipson, "Optical bistability on a silicon chip," *Opt. Lett.*, vol. 29, no. 20, pp. 2387–2389, 2004.
- [40] Q. Xu and M. Lipson, "Carrier-induced optical bistability in silicon ring resonators," *Opt. Lett.*, vol. 31, no. 3, pp. 341–343, 2006.
- [41] R. C. Alferness and R. V. Schmidt, "Tunable optical waveguide directional coupler filter," *Appl. Phys. Lett.*, vol. 33, no. 2, pp. 161–163, 1978.
- [42] X. Zhang, T. Zhang, C. Ji, F. Chu, T. Wang, and Y. Cui, "Optimized design for tunable optical waveguide ring resonator integrated with thermooptic Mach-Zehnder interferometer," *Acta Opt. Sinica*, vol. 28, no. 2, pp. 285–289, 2008.
- [43] X. Cao, S. Zheng, Y. Long, Z. Ruan, Y. Luo, and J. Wang, "Mesh-structure-enabled programmable multitask photonic signal processor on a silicon chip," *ACS Photon.*, vol. 7, no. 10, pp. 2658–2675, 2020.
- [44] W. Zhang, L. Zhou, Y. Xu, Z. Zhao, and S. Zheng, "Optical spectral shaping based on reconfigurable integrated microring resonator-coupled Fabry-Perot cavity," *J. Light. Technol.*, vol. 40, no. 22, pp. 7375–7382, Nov. 2022.
- [45] N. Zhou, S. Zheng, Y. Long, Z. Ruan, L. Shen, and J. Wang, "Reconfigurable and tunable compact comb filter and (de) interleaver on silicon platform," *Opt. Exp.*, vol. 26, pp. 4358–4369, 2018.
- [46] W. Shen, G. Zhou, J. Du, L. Zhou, K. Xu, and Z. He, "High-speed silicon microring modulator at the 2 μm waveband with analysis and observation of optical bistability," *Photon. Res.*, vol. 10, no. 3, pp. A35–A42, 2022.